Journal of Materials Chemistry A

PAPER

View Article Online
View Journal | View Issue

Cite this: J. Mater. Chem. A, 2017, 5, 25625

Carbon coated bimetallic sulfide nanodots/carbon nanorod heterostructure enabling long-life lithium-ion batteries†

Xuejie Gao,‡[a] Jiwei Wang,‡[b] Duo Zhang,[c] Keegan Adair,[b] Kun Feng,[a] Na Sun,[a] Hechuang Zheng,[a] Huiyun Shao,[a] Jun Zhong,[a] Yanyun Ma,*[a] Xueliang (Andy) Sun*[b] and Xuhui Sun*[a]

Received 3rd August 2017
Accepted 22nd November 2017

DOI: 10.1039/c7ta06849b

rsc.li/materials-a

Exploitation of high capacity and long-life anode materials is essential for the development of lithium-ion batteries (LIBs) with high energy density. Metal sulfides have shown great potential as anode materials for LIBs due to their high theoretical specific capacity and excellent electronic properties and therefore they are considered as excellent candidates for anode materials. However, structural degradation during cycling and polysulfide dissolution has limited their practical application. In this work, we design a unique 0D/1D heterostructure of carbon coated iron–nickel sulfide nanodots/carbon nanorod through simultaneous decomposition and sulfidation of a bi-metal organic framework template. The resultant nanodots/nanorod heterostructure allows for fast ion/electron transport kinetics, suppresses polysulfide dissolution and ensures structural integrity during the lithiation/delithiation process. Consequently, this carbon coated iron–nickel sulfide nanodots/carbon nanorod structure exhibits a high specific capacity (851.3 mA h g^{-1} at 0.5C after 200 cycles) and an excellent cycling stability (484.7 mA h g^{-1} after 1000 cycles at a high rate of 4C).

Introduction

The issues of global warming and depletion of fossil fuels have stimulated the search for clean and renewable energy sources, such as solar, wind, hydro and tidal energies. Additionally, the development of new energy storage technologies for sustainable energy sources has received great attention in recent times. Lithium-ion batteries (LIBs) possess high power and capacity, making them one of the most prominent and well-developed energy storage systems. However, commercialized LIBs utilize a graphite-based anode, which limits the theoretical energy density and is unable to satisfy the increasing demand for future high-energy storage applications. To achieve high-capacity anodes, metal sulfides (MSs) have been proposed and extensively investigated owing to their high theoretical specific capacity and excellent electronic properties.[1–7] However, their practical application has been restricted by rapid capacity fading and low rate performance due to the unstable structure and unsatisfactory electrochemical reaction kinetics during the lithiation/delithiation process.[8–10] Additionally, the dissolution of polysulfides (Li_2S_n, $n \geq 2$) into the electrolyte would lead to severe capacity fading.[11–14]

Considerable efforts have been devoted to addressing the aforementioned problems. Previous studies have proven that the reduction of the particle size to the nanoscale could significantly increase the Li^+ diffusion rate, ensuring a high rate performance.[2,15] Meanwhile, at the nanoscale, the mechanical strain generated during the repeated Li^+ insertion/extraction process can be well accommodated, thus inhibiting the pulverization of electrode materials caused by large volume changes. However, nano-sized particles are prone to aggregation during cycling, and thus the cycling performance is limited. The combination of nanoparticles with a carbon matrix (graphene,[16,17] carbon nanotubes,[11,18] and carbon nanosheets[19]) is an effective strategy to ensure uniform distribution of ultra-small nanoparticles as well as improve the electron conductivity. For example, Wang and co-workers reported a unique Co–Zn–S/C–CNT composite structure, in which Co–Zn–S nanoparticles were uniformly dispersed in the carbon matrix, exhibiting a high capacity and excellent rate performance.[20] Furthermore, embedment of MS active materials into conducting matrices could suppress polysulfide dissolution into the electrolyte, thus extending the cycling life.[11,14] Although

[a]Institute of Functional Nano and Soft Materials (FUNSOM), Jiangsu Key Laboratory for Carbon-Based Functional Materials and Devices, Collaborative Innovation Center of Suzhou Nano Science and Technology, Soochow University, Suzhou 215123, China. E-mail: mayanyun@suda.edu.cn; xhsun@suda.edu.cn

[b]Department of Mechanical and Materials Engineering, University of Western Ontario, London, Ontario, N6A 5B8, Canada. E-mail: xsun9@uwo.ca

[c]School for Radiological and Interdisciplinary Sciences (RAD-X), Soochow University, Suzhou 215123, China

† Electronic supplementary information (ESI) available. See DOI: 10.1039/c7ta06849b

‡ Xuejie Gao and Jiwei Wang contributed equally to this work.

these approaches are promising for high performance LIBs, the performance of MS anodes is still unacceptable due to the great challenges of simultaneously controlling the structure and properties.

Herein, we design a unique 0D/1D composite of carbon coated iron–nickel sulfide nanodots anchored on carbon nanorods (denoted as C@FeNi–S NDs/CNR) through the simultaneous decomposition and sulfidation of a metal organic framework (MOF), the glucose wrapped CH_4N_2S@Fe_2Ni MIL-88. The resulting nanostructure could enable a superior Li^+ storage performance due to several distinct advantages: (1) the ultra-small FeNi–S nanodots derived from the reaction between the Fe_2Ni MIL-88 and thiourea could greatly shorten the Li^+ diffusion length and provide additional electroactive sites; (2) the carbon nanorod backbone structure can ensure homogeneous dispersion of the FeNi–S nanodots as well as act as a conducting framework for efficient electron transport; (3) the thin outer carbon layer coated on the FeNi–S nanodots could effectively suppress the aggregation and dissolution of polysulfide intermediates during the Li^+ storage process. Thus, the designed C@FeNi–S NDs/CNR heterostructure exhibits an ultra-long cycling stability and excellent rate performance when evaluated as an anode material for LIBs.

Results and discussion

The preparation of C@FeNi–S NDs/CNR is schematically illustrated in Fig. 1. First, Fe_2Ni MIL-88 nanorods were synthesized *via* a hydrothermal method from a mixture solution of iron nitrate, nickel nitrate and 1,4-benzenedicarboxylic acid. The as-grown Fe_2Ni MIL-88 template was then mixed with thiourea, forming CH_4N_2S@Fe_2Ni MIL-88 composites. Glucose wrapped CH_4N_2S@Fe_2Ni MIL-88 nanorods were obtained by mixing the composites with glucose in ethanol solution. When the obtained composite powder is annealed in an Ar atmosphere at 600 °C, the organic ligands in the MOF (MIL-88) backbone are carbonized into carbon nanorods, and the CH_4N_2S will function as a sulfur source which reacts with the iron and nickel elements in the MOF structure. An optimal C@FeNi–S NDs/CNR heterostructure was finally obtained with a controlled annealing time of 2 h. For comparison, FeNi–S NPs/CNR was also synthesized through a synthetic method similar to that of C@FeNi–S NDs/CNR but without the introduction of glucose into the CH_4N_2S@Fe_2Ni MIL-88 nanorod precursor.

As a structural template, the metal–organic frameworks (MOFs) of Fe_2Ni MIL-88 were synthesized through a hydrothermal method according to the reported work,[21] exhibiting a uniform rod-like morphology with an average diameter of 30–60 nm and a length of approximately 600 nm (Fig. 2a). The corresponding X-ray diffraction (XRD) pattern in Fig. 2c shows distinct diffraction peaks that are well indexed to the Fe_2Ni MIL-88 phase (JCPDS no. 00-050-1789) and match with previously reported results, confirming that the as-prepared nanorods are phase-pure Fe_2Ni MIL-88 with high crystallinity. After mixing the Fe_2Ni MIL-88 nanorods with thiourea in ethanol solution, the diameter of the nanorods becomes slightly larger than that of the pristine sample owing to the thiourea molecular absorption on the nanorods (Fig. S1a†). The CH_4N_2S@Fe_2Ni MIL-88 composites were then further coated with a thin layer of glucose by uniformly mixing them together in ethanol, leading to uniform wrapping of the nanorods by glucose with the structural morphology remaining intact (Fig. S1b†). The C@FeNi–S NDs/CNR was obtained after carbonization and sulfidation of the glucose wrapped CH_4N_2S@Fe_2Ni MIL-88 precursor in an Ar atmosphere. Fig. 2b shows the structural features of the as-prepared C@FeNi–S NDs/CNR and reveals that the calcination process does not destroy the morphology of the Fe_2Ni MIL-88 nanorods, while the surface adopts a rougher quality due to the formation of ultra-small FeNi–S nanodots on the carbon nanorod surface. The corresponding XRD pattern (Fig. 2d) is in good agreement with the hexagonal FeNi–S (JCPDS no. 00-050-1789). For comparison, the CH_4N_2S@Fe_2Ni MIL-88 nanorod precursor was calcined under the same

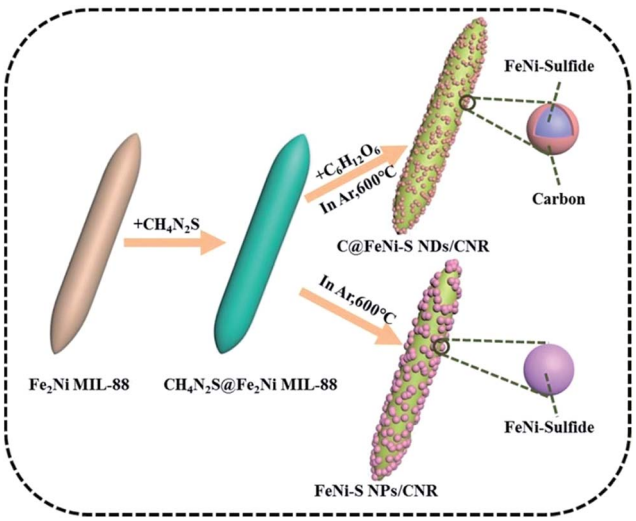

Fig. 1 Schematic illustration of the synthesis of C@FeNi–S NDs/CNR and FeNi–S NPs/CNR.

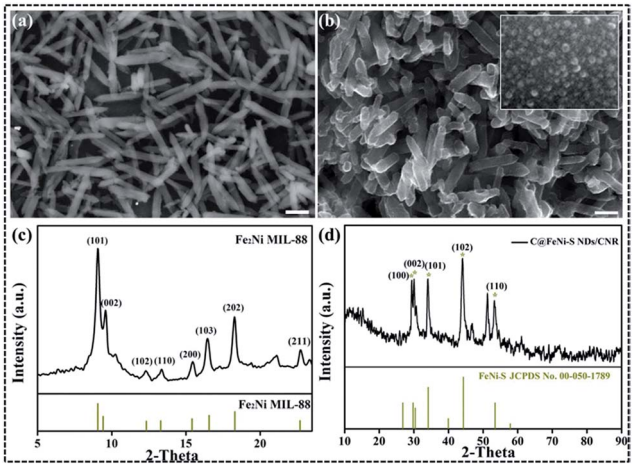

Fig. 2 SEM images and XRD patterns of the as-synthesized Fe_2Ni MIL-88 nanorods (a and c) and C@FeNi–S NDs/CNR (b and d). Scale bar in (a and b): 200 nm.

synthetic conditions without the introduction of glucose, resulting in the product FeNi–S NPs/CNR. Although the obtained product still possesses a nanorod structure with the surface decorated by nanoparticles, the particle size is much larger (around 9–13 nm) with a random distribution (Fig. S2a†). Additionally, the XRD pattern of FeNi–S NPs/CNR (Fig. S2b†) can be indexed to FeNi–S (JCPDS no. 00-020-0533). The comparison between the two products reveals that the addition of glucose plays a significant role in controlling the iron–nickel sulfide morphology and phase structure.

In order to investigate the effect of annealing time on the morphology of the final product, the glucose wrapped CH_4N_2-S@Fe_2Ni MIL-88 nanorods were calcined at 600 °C for different time periods of 1 h and 3 h in Ar. With 1 h of annealing, the product could retain the nanorod morphology with only a few nanoparticles on the carbon nanorod surface (Fig. S3a†). As the annealing time increased to 3 h, the surface of the product became much rougher due to the complete reaction between the Fe_2Ni MIL-88 and thiourea. Although part of the product still retained the rod-like morphology, most of the nanorods aggregated to form a bulk structure, and more aggregation of the FeNi–S nanoparticles was also observed clearly (Fig. S3b†). The optimized annealing time of 2 h was proven well.

TEM characterization was conducted to further study the detailed morphology and structure of the obtained C@FeNi–S NDs/CNR. The low magnification TEM image of the C@FeNi–S NDs/CNR clearly shows a rod-like morphology with a diameter of around 80 nm, and it can be seen that numerous uniform FeNi–S nanodots are homogeneously distributed on the surface (Fig. 3a and S4†). The magnified TEM image (Fig. S4b†) illustrates that the FeNi–S nanodots are very small (3–6 nm) with a narrow diameter distribution. It is worth noting that the nanodots are coated with a thin layer of carbon (1–2 nm) as shown in Fig. 3b and S4c.† As a comparison, the TEM characterization (Fig. S5a†) shows that the FeNi–S nanoparticles partially aggregate without the coating of a thin carbon layer, and the particle size is larger with a diameter of 9–13 nm (Fig. S5b†). The high-resolution TEM (HRTEM) image of the regional C@FeNi–S NDs/CNR in Fig. 3b reveals clear lattice fringes with the space distances of 0.204 nm, 0.267 nm and 0.298 nm which could be indexed to the (102), (101) and (100) planes of FeNi-sulfide, respectively. The inset of the selected area electron diffraction (SAED) pattern shows a ring-like diffraction, suggesting a polycrystalline structure of the C@FeNi–S NDs/CNR. Furthermore, the STEM mode image and the corresponding elemental mapping (Fig. 3c–g) confirmed the uniform distribution of C, Fe, Ni and S elements throughout the carbon nanorod structure.

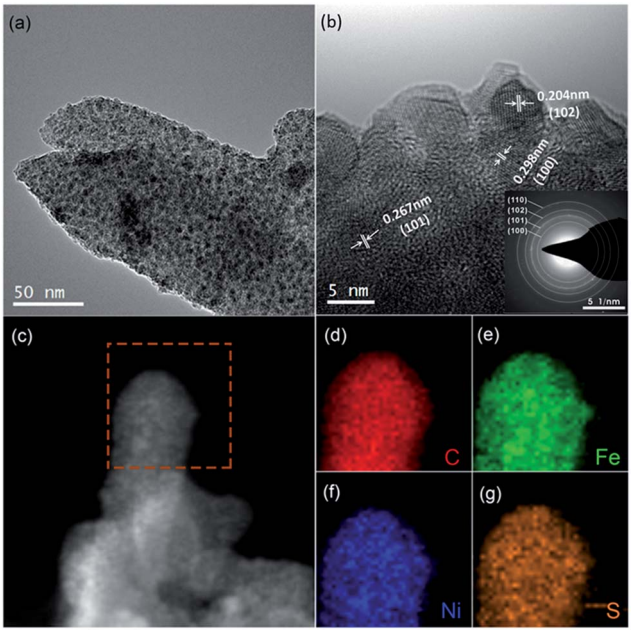

Fig. 3 TEM image (a), HRTEM image and indexed SAED pattern (inset) (b), and elemental mapping images (c–g) of C@FeNi–S NDs/CNR.

The carbon content in the C@FeNi–S NDs/CNR nanocomposite was determined by thermal gravimetric analysis (TGA) with heating in the range of 25 °C to 600 °C under an oxygen environment (Fig. S6a†). The carbon and FeNi-sulfide were completely oxidized to CO_2, presenting a total weight loss of 51.07%, suggesting that the carbon content in the composite is 23.3%. Furthermore, Raman analysis was carried out to investigate the carbon structure of C@FeNi–S NDs/CNR (Fig. S6c†). The Raman spectrum presents two characteristic peaks located at about 1334 cm^{-1} and 1591.9 cm^{-1}, which could be assigned to the D band and the G band of carbon, respectively. The peak intensity ratio between the D band and the G band (I_D/I_G) is around 1.11, implying that the carbon in the composites has an amorphous structure.[21] The FeNi–S NPs/CNR shows a similar Raman feature with an I_D/I_G ratio of 1.06, which also suggests that the carbon nanorods were amorphous.

For further analysis of the nanocomposites, XPS was applied to examine the chemical states of C@FeNi–S NDs/CNR. The survey spectrum in Fig. S7a† shows the characteristic peaks of Fe, Ni, S, O, and C, indicating the coexistence of these elements and good agreement with the STEM mapping results. The Fe 2p spectrum (Fig. S7b†) shows two peaks at 711.2 eV ($2p_{3/2}$) and 724.4 eV ($2p_{1/2}$), which proves that the Fe is divalent in the C@FeNi–S NDs/CNR. Furthermore, the Ni 2p spectrum as shown in Fig. S7c† exhibits two peaks located at 855.8 eV and 863.2 eV, which could be assigned to Ni^{2+}.[22] In the S 2p spectrum (Fig. S7d†), the peak observed at 163.7 eV is related to S $2p_{3/2}$ of the C–S–C covalent bond of the thiophene–S arising from spin–orbit coupling.[23] In addition, the intense peak located at 168.2 eV can be indexed to oxidized sulfur groups (–C–SO_x–C–, x = 2–4), such as sulfate or sulfonate.[24]

In order to understand in depth the chemical states of the C@FeNi–S NDs/CNR and FeNi–S NPs/CNR as anode materials, the X-ray absorption spectroscopy (XAS) technique as a sensitive local environment tool was used to clarify the electronic structure of C@FeNi–S NDs/CNR compared with that of the FeNi–S NPs/CNR. The C K-edge spectra of FeNi–S NPs/CNR and C@FeNi–S NDs/CNR are displayed in Fig. 4a to reflect the difference between the two composites, and the reduced absorption peak of graphitic characteristics at about 284.5 eV (labeled A) and the increased absorption peak of oxidized carbon at about 287.7 eV (labeled B) in the C@FeNi NDs/CNR

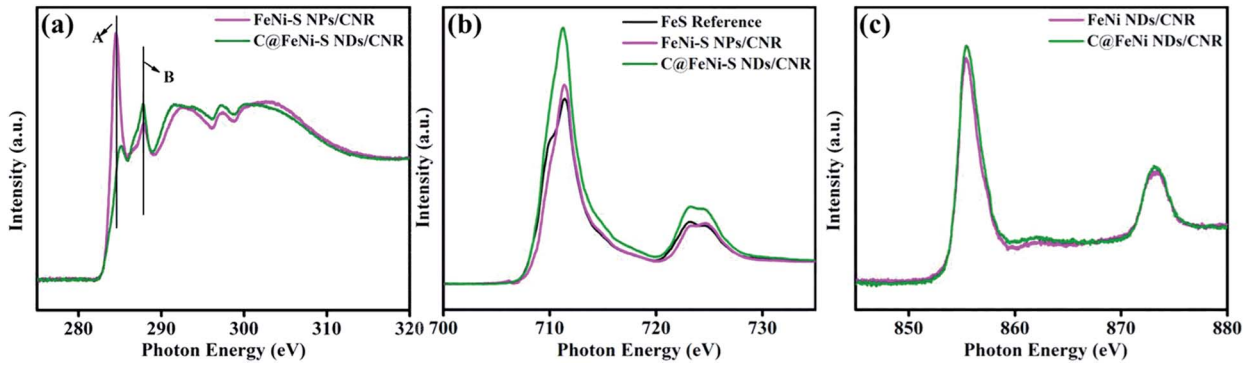

Fig. 4 XAS spectra of the C@FeNi–S NDs/CNR and FeNi–S NPs/CNR: (a) C K-edge; (b) Fe $L_{2,3}$-edge; (c) Ni $L_{2,3}$-edge.

composite further indicate that the coated carbon layer is amorphous and bonded to S. The chemical states of Fe and Ni of C@FeNi–S NDs/CNR modified by glucose were investigated by Fe and Ni $L_{2,3}$-edge spectra, as shown in Fig. 4b and c. The $L_{2,3}$-edge of the 3d transition metals (Fe and Ni) results from the electronic transition from the 2p level to the unoccupied 3d states.[25] Both Fe and Ni $L_{2,3}$-edge spectra show Fe^{2+} and Ni^{2+} characteristics, respectively, which is consistent with the XPS results. Compared with those of FeNi NPs/CNR, the increase in the spectral intensity of the Fe and Ni L-edge indicates more unoccupied Fe(3d) and Ni(3d) states,[26] which clearly means the chemical interaction between FeNi–S NDs and the carbon thin film formed from glucose, possibly promoting the conductivity of FeNi–S NDs.

The Li^+ storage performance of the C@FeNi–S NDs/CNR composite as the anode material for LIBs was evaluated. Fig. 5a shows the typical cyclic voltammogram (CV) with a scan rate of 0.1 mV s^{-1} in the voltage range of 0.01–3.0 V. In the first cathodic scan, there are two small peaks at around 1.71 V and 1.32 V, corresponding to the formation of Li_2FeS_2 by lithium insertion and its conversion to Li_2S and Fe.[27] Another two peaks at around 0.96 V and 0.77 V can be ascribed to the reduction of FeNi-sulfide to Fe and Ni and the formation of the solid electrolyte interface (SEI) film on the surface of the electrode.[28] In the anodic sweep, the strong peak at around 1.92 V could be assigned to the reversible oxidation of metal to metal sulfides. In the subsequent cycles, the cathodic peaks overlap well, proving the excellent stability of the C@FeNi–S NDs/CNR heterostructure. However, FeNi–S NPs/CNR shows a different CV curve (Fig. S8a†) with a small peak present at 1.70 V, indicating the pre-lithiation of FeS, followed by a single intense peak at 0.75 V which could be attributed to the formation of a solid electrolyte interface (SEI) due to electrolyte decomposition. In addition, a small broad peak appears at about 1.60 V in the second cycle, which corresponds to the lithiation of metallic Ni. On the anodic side, Ni and Fe oxidation reactions to NiS and FeS could be observed at 1.65 V and 2.35 V, respectively. The characteristic peaks in the subsequent CV curves of FeNi–S NPs/CNR do not overlap well compared to those of C@FeNi–S NDs/CNR, suggesting that FeNi–S NPs/CNR is less stable and susceptible to capacity fade.

Fig. 5b shows the galvanostatic charge–discharge curves of C@FeNi–S ND/CNR over 200 cycles at a rate of 0.5C within the voltage range of 0.01–3.0 V. The discharge and charge capacities in the first cycle were 905 and 820 mA h g^{-1}, respectively, leading to a high coulombic efficiency (CE) of 90.61%. This high initial CE benefits from the advantages of the special carbon coated FeNi–S nanodots/carbon nanorod heterostructure, ensuring good reversible lithiation/delithiation processes. The subsequent discharge/charge curves overlap well with the curve

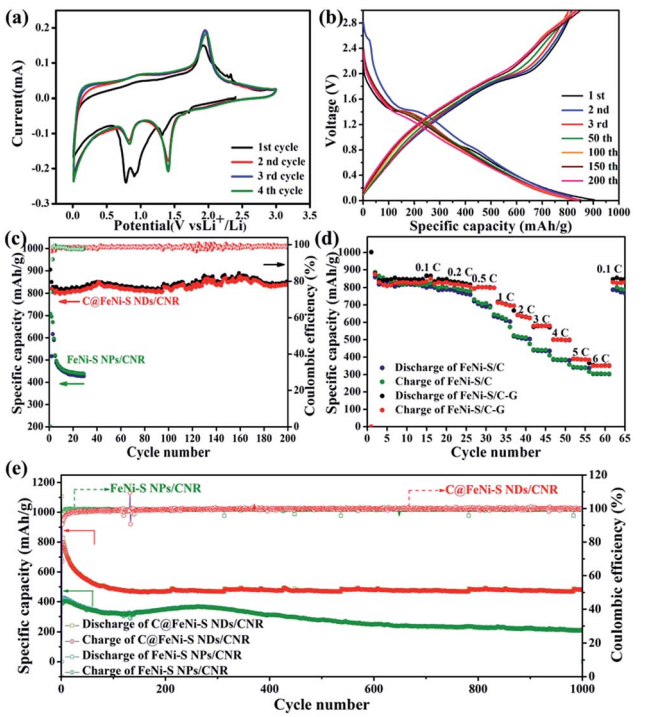

Fig. 5 (a) CV curves at a scan rate of 0.1 mV s^{-1} for the initial four cycles of C@FeNi–S NDs/CNR; (b) galvanostatic charge–discharge voltage profiles for different cycles at a rate of 0.5C for C@FeNi–S NDs/CNR; (c) electrochemical performance comparison of capacity retention and coulombic efficiency between C@FeNi–S NDs/CNR and FeNi–S NPs/CNR at the rate of 0.5C for 200 cycles; (d) comparison of rate performance at different current rates; (e) capacity retention of C@FeNi–S NDs/CNR and FeNi–S NPs/CNR at a rate of 4C for 1000 cycles. Voltage range: 0.01–3.0 V *vs.* Li/Li^+.

in the first cycle, indicating the excellent reversibility and structural stability of the C@FeNi–S ND/CNR electrode. In contrast, the galvanostatic charge–discharge curves of FeNi–S NPs/CNR composites for different cycles (1st, 2nd, 3rd and 20th) at a rate of 0.5C (Fig. S8b†) obviously show that the corresponding coulombic efficiency was much lower than that of C@FeNi–S NDs/CNR. Thus, C@FeNi–S NDs/CNR could not only highly enhance the conductivity by providing a continuous conductive network, but also effectively mitigate the large volume expansion due to the carbon coating *via* the carbonization of the glucose.[27,29]

Fig. 5c shows the cycling performance of the C@FeNi–S NDs/CNR and FeNi–S NPs/CNR composites at a rate of 0.5C. The C@FeNi–S NDs/CNR exhibits a high specific capacity of 851.3 mA h g^{-1} even after 200 cycles, with 94% retention of the initial discharge capacity. Moreover, the CE could stabilize at approximately 99% after 200 cycles, demonstrating the good cycling stability of the C@FeNi–S NDs/CNR. In contrast, the FeNi–S NPs/CNR exhibits fast capacity fading during the first few cycles, and only displays a capacity of around 420 mA h g^{-1} after 30 cycles, which is much lower than that of the C@FeNi–S NDs/CNR. The rate capabilities of the C@FeNi–S NDs/CNR and FeNi–S NPs/CNR were further compared at various rates as shown in Fig. 5d. It seems that the two materials present close reversible capacities at low rates (0.1C and 0.2C), but the C@FeNi–S NDs/CNR exhibits much higher capacities than FeNi–S NPs/CNR at high rates. The specific capacities of the C@FeNi–S NDs/CNR were 801.4 mA h g^{-1}, 696.8 mA h g^{-1}, 624.6 mA h g^{-1}, 582.03 mA h g^{-1}, 498.2 mA h g^{-1}, 382.81 mA h g^{-1} and 346.09 mA h g^{-1} at 0.5C, 1C, 2C, 3C, 4C, 5C and 6C, respectively. More importantly, a high capacity of 820 mA h g^{-1} can be achieved when the rate returns to 0.1C, further suggesting the good reversibility of the C@FeNi–S NDs/CNR anode. However, the specific capacities of the FeNi–S NPs/CNR were much lower than those of C@FeNi–S NDs/CNR. In addition to high specific capacity and good rate performance, long cycle life is also a significant factor for the practical application, and thus, the long-term cycling performance of the C@FeNi–S NDs/CNR and FeNi–S NPs/CNR was also explored and compared at a very high rate of 4C (Fig. 5e). For C@FeNi–S NDs/CNR, a high reversible capacity of 484.7 mA h g^{-1} can be obtained at 4C after 1000 cycles, with a very small capacity fade rate of 0.04% per cycle. In comparison, FeNi–S NPs/CNR only had a capacity of 212.1 mA h g^{-1} after 1000 cycles. Moreover, the CE of the C@FeNi–S NDs/CNR remains at nearly 100% during the 1000 cycles while the CE of FeNi–S NPs/CNR is a little bit lower, suggesting that the thin carbon layer could ensure a higher CE value and stabilize the encapsulated metal sulfide nanoparticles. Even at a higher rate of 6C, the C@FeNi–S NDs/CNR electrode could still display a specific capacity of 361.0 mA h g^{-1} after 1000 cycles, without any capacity fading after the first few cycles (Fig. S9†). In order to investigate the structural stability of the C@FeNi–S NDs/CNR and FeNi–S NPs/CNR electrodes during Li^+ insertion/extraction, TEM images of the electrode (Fig. S10†) were taken after 200 cycles at 0.5C. In contrast to Fig. S10a,† Fig. S10b† reflected that the C@FeNi–S NDs/CNR electrode maintains the rod structure even after 200 cycles and nanodots are clearly observed in Fig. S9b,† revealing the structural stability of this anode during the cycling process.

In order to understand the reaction mechanism of the C@FeNi–S NDs/CNR during the cycling,[30–32] *ex situ* XRD measurements of the C@FeNi–S NDs/CNR electrodes were performed and the XRD patterns are shown in Fig. S11.† In general, the FeNi–S can be reduced to metals and Li_2S during the discharge process. As presented in XRD patterns, the characteristic peaks in the pristine FeNi–S almost disappear after the discharge/charge process, and only a weak iron sulfide peak remained when discharged to 1.5 V; with the discharge process continuing, the weak iron sulfide peak almost disappeared. In the charge process, the iron sulfide peak appears again when charged to 3.0 V. There are no peaks related to nickel sulfide, suggesting that the reduced Ni metal might have acted as a buffer matrix during the whole cycling process. Moreover, no metal peaks were detected from the XRD patterns at various states, which indicates that the reduced metal was present in an amorphous state.[3,33–35]

Electrochemical impedance spectroscopy (EIS) of C@FeNi–S NDs/CNR and FeNi–S NPs/CNR (Fig. S12†) was performed to analyze their interfacial impedance. As can be seen, all curves show a semicircle at a high frequency and a short line at a low frequency, corresponding to the charge-transfer resistance (R_{ct}) and Warburg impedance, respectively.[36–39] The C@FeNi–S NDs/CNR shows a smaller R_{ct} (65.69 Ω, obtained from the equivalent circuit shown in Fig. S13†) and a steeper line compared with its counterpart (FeNi–S NPs/CNR, 75.19 Ω), suggesting increased electrochemical activity and fast Li^+ diffusion after carbon coating.[40–43] This is the main reason that leads to higher capacity output and lower electrode pulverization during the charge and discharge process, which coincides well with the anode performance as shown in Fig. 5c and d. After cycling, the increased diameter of the semicircle and the decreased slope of the short line for both anodes shown in Fig. S12b† indicate that the electrochemical activity and Li^+ diffusion capability decreased during the charge/discharge process because of the structural change. Nevertheless, it is still noteworthy that the difference of both the R_{ct} and the slope of the line between C@FeNi–S NDs/CNR (183.90 Ω) and FeNi–S NDs/CNR (475.30 Ω) is further enlarged compared with that of the anodes before cycling. This situation can be explained as follows. For FeNi–S NPs/CNR, the size of FeNi–S-NPs increased a lot during cycling (Fig. S10†), which reduced the electrochemical activity and prolonged the Li^+ diffusion distance, while the size of FeNi–S-NDs in C@FeNi–S NDs/CNR was maintained well due to the carbon coating; this further highlighted the important role of the carbon coating in stabilizing the electrochemical performance.[36] In contrast to other reported TMS (Transitional Metal Sulfide) based anodes in LIBs as summarized in Table S1,† the C@FeNi–S NDs/CNR in this work shows the best cycling performance with high capacity and long cycle life, in particular, at high rates such as 4C and 6C.

The excellent electrochemical performance of the C@FeNi–S NDs/CNR, especially the long-cycle stability and high rate capability, can be attributed to the following factors. First, the ultra-small FeNi–S NDs (3–6 nm) enable a short diffusion path

length and fast Li^+ transport during charge and discharge process, rendering a high rate performance. Meanwhile, it can also mitigate mechanical strain and improve the availability of the anode material during the cycling process. Second, the thin layer of carbon on the outer surface can not only suppress the dissolution of polysulfide intermediates, but also form interconnected conductive paths between the ultra-small nanodots, ensuring fast electron transfer. Furthermore, the 1D carbon nanorods could effectively promote the homogeneous dispersion of the FeNi–S NDs and serve as a continuous conducting network, thus avoiding particle aggregation and favoring efficient electron transport. Moreover, the 1D carbon backbone plays an important role in maintaining structural integrity during cycling.

Experimental

Synthesis of Fe_2Ni MIL-88 nanorods

Fe_2Ni MIL-88 nanorods were prepared using a hydrothermal method according to previous work.[44] Typically, 48 mg of $Ni(NO_3)_2 \cdot 6H_2O$, 90.5 mg of $FeCl_3 \cdot 6H_2O$ and 83.1 mg of 1,4-benzenedicarboxylic acid (H_2bdc) were mixed in 5 mL dimethyl formamide (DMF) under vigorous stirring until the color of the solution became transparent brown-yellow. Subsequently, 2 mL of NaOH solution (0.2 M) was added to the mixture with another 15 min stirring, resulting in a brown-yellow suspension. Afterwards, the suspension was transferred into a 50 mL Teflon-lined autoclave and heated at 100 °C for 15 h. After cooling to room temperature, the resulting yellow product was collected by centrifugation, washed with ethanol several times, and then dried at 70 °C overnight.

Synthesis of FeNi–S NPs/CNR

In a typical synthesis, 270 mg of Fe_2Ni MIL-88 and 320 mg of CH_4N_2S were added to 200 mL ethanol under ultrasonication for 15 min and then stirred for 24 h, followed by evaporating the ethanol at 60 °C for 12 h. To obtain the FeNi–S NPs/CNR structure, the CH_4N_2S@Fe_2Ni MIL-88 mixture powder was heated at 600 °C for 2 h under Ar flow, at a heating rate of 2 °C min^{-1}.

Synthesis of C@FeNi–S NDs/CNR

Typically, stoichiometric ratios of the as-synthesized Fe_2Ni MIL-88 (91.5 mg), N_2H_4S (108.5 mg) and glucose (60 mg) were mixed in 40 mL of alcohol and then stirred for 24 h. Afterwards, the solution was dried at 60 °C for 12 h. To obtain the C@FeNi–S NDs@CNR structure, the dried powder was heated at 600 °C for 2 h under Ar flow at a heating rate of 2 °C min^{-1}.

Characterization

Scanning electron microscopy (SEM, Zeiss-supra 55 with acceleration voltage of 10 kV) and transmission electron microscopy (TEM, FEI Quanta FRG 200 F, operating at 200 kV) were employed to characterize the morphology and crystal structure of the as-prepared nanocomposites. X-ray diffraction (XRD, Empyrean, Cu Kα) was utilized to investigate the crystalline phase of the product. Thermogravimetric analysis (Switzerland TGA1) was used to determine the carbon content in the nanocomposites at a heating rate of 10 °C min^{-1} in air from room temperature to 1000 °C. X-ray photoelectron spectroscopy (XPS, Kratos AXIS ULTRADLD) was performed to study the chemical states of the nanocomposites. Raman (Lab RAMHR800) spectra were recorded to evaluate the carbon structure. Synchrotron based X-ray absorption spectroscopy (XAS) was performed to investigate the electronic structure of the samples on the beam line 20 A at Taiwan Light Source (TLS).

Electrochemical measurements

Electrochemical tests were carried out using CR 2032 coin cells. The active material, carbon black, and polyvinylidene fluoride (PVDF) binder were mixed in a weight ratio of 70 : 20 : 10. Afterwards, the slurry was coated on Cu foil and dried at 70 °C for 12 h under vacuum. The mass loadings of active materials were about 1.3 mg cm^{-2}. The cells were assembled in an Ar-filled glove box with Li foil as counter and reference electrodes and a porous polypropylene film as the separator. The electrolyte solution was 1 M $LiPF_6$ in a mixture of ethylene carbonate (EC), diethyl carbonate (DEC) and dimethyl carbonate (DMC) (1 : 1 : 1 by volume). The galvanostatic charge–discharge performance was evaluated with a LAND test system within a voltage range of 0.01–3 V (*vs.* Li/Li^+). Cyclic voltammetry was performed between 0.01 and 3 V at a scan rate of 0.1 mV s^{-1}. Electrochemical impedance spectroscopy (EIS) was carried out in the frequency range from 100 000 to 0.01 Hz with an AC voltage of 5 mV amplitude. The specific capacities were calculated based on the total weight of carbon and iron–nickel sulfide active materials.

Conclusions

In summary, a unique structure of carbon-coated iron–nickel sulfide nanodots/carbon nanorod (C@FeNi–S NDs/CNR) was prepared through simultaneous decomposition and sulfidation of a bimetallic organic framework template. When evaluated as an anode material for LIBs, the as-obtained C@FeNi–S NDs/CNR heterostructure exhibited an exceptional reversible capacity of 851.3 mA h g^{-1} at 0.5C after 200 cycles and excellent cycling stability (484.7 mA h g^{-1} after 1000 cycles at a high rate of 4C). Our work presents an effective way to realize a novel 0D/1D bimetallic sulfide/carbon heterostructure including the merits of fast ion/electron reaction kinetics, polysulfide suppression and structural integrity, which would shed light on the development of next-generation LIB-based metal sulfide anodes.

Conflicts of interest

There are no conflicts to declare.

Acknowledgements

X. G. and J. W. contributed equally to this work. This work was supported by the Natural Science Foundation of China (NSFC)

(Grant No. U1432249), the National Key R&D Program of China (Grant 2017YFA0205002) and the Priority Academic Program Development (PAPD) of Jiangsu Higher Education Institutions. This is also a project supported by Jiangsu Key Laboratory for Carbon-Based Functional Materials and Devices and Collaborative Innovation Center of Suzhou Nano Science & Technology.

Notes and references

1 H. Li, Y. Gao, Y. Shao, Y. Su and X. Wang, *Nano Lett.*, 2015, **15**, 6689–6695.
2 N. Mahmood, C. Zhang and Y. Hou, *Small*, 2013, **9**, 1321–1328.
3 Z. Xu, H. Wang, Z. Li, A. Kohandehghan, J. Ding, J. Chen, K. Cui and D. Mitlin, *J. Phys. Chem. C*, 2014, **118**, 18387–18396.
4 Y. Zhou, D. Yan, H. Xu, J. Feng, X. Jiang, J. Yue, J. Yang and Y. Qian, *Nano Energy*, 2015, **12**, 528–537.
5 R. Wu, D. P. Wang, X. Rui, B. Liu, K. Zhou, A. W. Law, Q. Yan, J. Wei and Z. Chen, *Adv. Mater.*, 2015, **27**, 3038–3044.
6 C. Wang, M. Lan, Y. Zhang, H. Bian, M.-F. Yuen, K. Ostrikov, J. Jiang, W. Zhang, Y. Y. Li and J. Lu, *Green Chem.*, 2016, **18**, 3029–3039.
7 Z. Wang, X. Li, Y. Yang, Y. Cui, H. Pan, Z. Wang, B. Chen and G. Qian, *J. Mater. Chem. A*, 2014, **2**, 7912.
8 G. D. Park, S. H. Choi, J. K. Lee and Y. C. Kang, *Chemistry*, 2014, **20**, 12183–12189.
9 W. Qiu, J. Jiao, J. Xia, H. Zhong and L. Chen, *Chemistry*, 2015, **21**, 4359–4367.
10 L. Yang, S. Wang, J. Mao, J. Deng, Q. Gao, Y. Tang and O. G. Schmidt, *Adv. Mater.*, 2013, **25**, 1180–1184.
11 L. Xu, Y. Hu, H. Zhang, H. Jiang and C. Li, *ACS Sustainable Chem. Eng.*, 2016, **4**, 4251–4255.
12 B. Wu, H. Song, J. Zhou and X. Chen, *Chem. Commun.*, 2011, **47**, 8653–8655.
13 X. Rui, H. Tan and Q. Yan, *Nanoscale*, 2014, **6**, 9889–9924.
14 Q. Wang, R. Zou, W. Xia, J. Ma, B. Qiu, A. Mahmood, R. Zhao, Y. Yang, D. Xia and Q. Xu, *Small*, 2015, **11**, 2511–2517.
15 P. G. Bruce, B. Scrosati and J. M. Tarascon, *Angew. Chem.*, 2008, **47**, 2930–2946.
16 S. Peng, X. Han, L. Li, Z. Zhu, F. Cheng, M. Srinivansan, S. Adams and S. Ramakrishna, *Small*, 2016, **12**, 1359–1368.
17 Y. Tan, M. Liang, P. Lou, Z. Cui, X. Guo, W. Sun and X. Yu, *ACS Appl. Mater. Interfaces*, 2016, **8**, 14488–14493.
18 Y. Xiao, J.-Y. Hwang, I. Belharouak and Y.-K. Sun, *ACS Energy Lett.*, 2017, **2**, 364–372.
19 Y. Xu, W. Li, F. Zhang, X. Zhang, W. Zhang, C.-S. Lee and Y. Tang, *J. Mater. Chem. A*, 2016, **4**, 3697–3703.
20 H. Li, Y. Su, W. Sun and Y. Wang, *Adv. Funct. Mater.*, 2016, **26**, 8345–8353.
21 J. T. Chen, K. Shin, J. M. Leiston-Belanger, M. Zhang and T. P. Russell, *Adv. Funct. Mater.*, 2006, **16**, 1476–1480.
22 A. A. AbdelHamid, X. Yang, J. Yang, X. Chen and J. Y. Ying, *Nano Energy*, 2016, **26**, 425–437.
23 X. Yu and H. S. Park, *Carbon*, 2014, **77**, 59–65.
24 C. H. Choi, S. H. Park and S. I. Woo, *Green Chem.*, 2011, **13**, 406–412.
25 J. Zhou, J. Wang, L. Zuin, T. Regier, Y. Hu, H. Wang, Y. Liang, J. Maley, R. Sammynaiken and H. Dai, *Phys. Chem. Chem. Phys.*, 2012, **14**, 9578–9581.
26 S. Shen, J. Zhou, C. L. Dong, Y. Hu, E. N. Tseng, P. Guo, L. Guo and S. S. Mao, *Sci. Rep.*, 2014, **4**, 6627.
27 P. Lou, Y. Tan, P. Lu, Z. Cui and X. Guo, *J. Mater. Chem. A*, 2016, **4**, 16849–16855.
28 M. V. Reddy, T. Yu, C. H. Sow, Z. X. Shen, C. T. Lim, G. V. Subba Rao and B. V. R. Chowdari, *Adv. Funct. Mater.*, 2007, **17**, 2792–2799.
29 S.-P. Guo, J.-C. Li, Z. Ma, Y. Chi and H.-G. Xue, *J. Mater. Sci.*, 2016, **52**, 2345–2355.
30 X. Fang, X. Guo, Y. Mao, C. Hua, L. Shen, Y. Hu, Z. Wang, F. Wu and L. Chen, *Chem.–Asian J.*, 2012, **7**, 1013–1017.
31 X. Fang, C. Hua, X. Guo, Y. Hu, Z. Wang, X. Gao, F. Wu, J. Wang and L. Chen, *Electrochim. Acta*, 2012, **81**, 155–160.
32 T. Stephenson, Z. Li, B. Olsen and D. Mitlin, *Energy Environ. Sci.*, 2014, **7**, 209–231.
33 J. Xiao, X. Wang, X.-Q. Yang, S. Xun, G. Liu, P. K. Koech, J. Liu and J. P. Lemmon, *Adv. Funct. Mater.*, 2011, **21**, 2840–2846.
34 X. Fang, X. Yu, S. Liao, Y. Shi, Y.-S. Hu, Z. Wang, G. D. Stucky and L. Chen, *Microporous Mesoporous Mater.*, 2014, **196**, 359.
35 J. Ding, Z. Li, H. Wang, K. Cui, A. Kohandehghan, X. Tan, D. Karpuzov and D. Mitlin, *J. Mater. Chem. A*, 2015, **3**, 7100–7111.
36 J. Pokrzywinski, J. K. Keum, R. E. Ruther, E. C. Self, M. Chi, H. Meyer Iii, K. C. Littrell, D. Aulakh, S. Marble, J. Ding, M. Wriedt, J. Nanda and D. Mitlin, *J. Mater. Chem. A*, 2017, **5**, 13511–13525.
37 X. Yang, N. Yan, W. Zhou, H. Zhang, X. Li and H. Zhang, *J. Mater. Chem. A*, 2015, **3**, 15314–15323.
38 X. Yang, Y. Yu, N. Yan, H. Zhang, X. Li and H. Zhang, *J. Mater. Chem. A*, 2016, **4**, 5965–5972.
39 D. Aurbach, E. Zinigrad, Y. Cohen and H. Teller, *Solid State Ionics*, 2002, **148**, 405–416.
40 D. Aurbach, *J. Power Sources*, 2000, **89**, 206–218.
41 D. Aurbach, M. D. Levi, E. Levi, H. Telier, B. Markovsky and G. Salitra, *J. Electrochem. Soc.*, 1998, **145**, 3024–3034.
42 X. Yang, H. Zhang, Y. Chen, Y. Yu, X. Li and H. Zhang, *Nano Energy*, 2017, **39**, 418–428.
43 D. Du, W. Yue, X. Fan, K. Tang and X. Yang, *Electrochim. Acta*, 2016, **194**, 17–25.
44 G. Huang, F. Zhang, L. Zhang, X. Du, J. Wang and L. Wang, *J. Mater. Chem. A*, 2014, **2**, 8048.